ACS Energy LETTERS

http://pubs.acs.org/journal/aelccp

Self-Absorbed Cage-like *o*-Carborane Atomic Cluster Derived Artificial Interphase for Aqueous Zinc-Ion Batteries

Yuge Feng,[#] Yaoda Wang,[#] Junchuan Liang, Lina Qin, Kaiqiang Zhang, Shuhong Xu, ChunLei Wang, and Zhong Jin*

Cite This: *ACS Energy Lett.* 2025, 10, 6489−6499

Read Online

ACCESS | Metrics & More | Article Recommendations | Supporting Information

ABSTRACT: **The practical deployment of rechargeable aqueous zinc-ion batteries is greatly hindered by severe Zn dendrite growth and the hydrogen evolution reaction on Zn metal anodes. Herein, we report the spontaneous construction of an adsorption-induced *o*-carborane artificial interphase to stabilize Zn anodes. The cage-structured *o*-carborane clusters possess robust structural stability and chemical inertness, endowing Zn anodes with strong durability to suppress Zn dendrite and hydrogen evolution. The constructed *o*-carborane protective layer can redistribute Zn^{2+} flux, avoiding nonuniform Zn deposition and achieving highly reversible Zn plating/stripping processes. The *o*-carborane-derived SEI can prevent Zn metal from being corroded by the electrolyte and accelerate Zn^{2+} transfer. Consequently, Zn||Zn symmetric batteries and Zn||Cu half-batteries based on *o*-carborane-modified Zn electrodes demonstrate long cycling lifespans at elevated current densities. The assembled Zn||V_2O_5 batteries also achieve lower voltage polarization, enhanced rate capability, and prolonged cycling stability. This work highlights the potential of adsorption-driven artificial interphases constructed from cage-like clusters in stabilizing transition metal anodes, providing a promising route to develop advanced aqueous multivalent-ion batteries.**

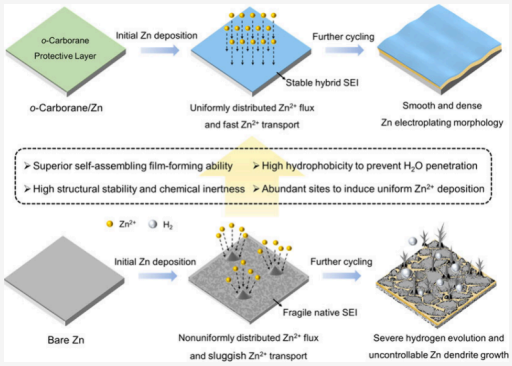

Zinc (Zn) metal has been considered a promising anode material for aqueous energy storage devices due to its low redox potential (−0.762 V vs standard hydrogel electrode), high specific capacity (820 mAh g^{-1} or 5854 mAh cm^{-3}), high natural abundance, and low toxicity.[1−3] Unfortunately, the development of rechargeable Zn-ion batteries is confronted with numerous rigorous challenges, including severe electrolyte corrosion and uncontrollable dendrite growth during the repeated Zn plating/stripping processes.[4−6] These issues greatly deteriorate the cycling stability and reversibility of the Zn metal anodes. To date, considerable efforts have been dedicated to addressing these challenges. Optimizing electrolyte compositions by additives or salts is considered a feasible strategy for forming a stable solid electrolyte interphase (SEI) to stabilize Zn metal anodes.[7−10] However, the continuous consumption of additives and salts during cycling compromises sustained interfacial stability and dendrite growth suppression. Employing hydrogel polymer electrolytes (HPEs) is demonstrated to be another effective strategy to promote uniform Zn deposition and reduce side reactions.[11−15] Nevertheless, the ionic conductivity and mechanical strength of HPEs still need to be further improved. Different from the above two approaches, constructing a robust and highly Zn^{2+}-conducting artificial interphase is another promising route to achieve highly durable Zn metal anodes. Recently, various artificial interfacial layers, including inorganic materials[16−25] and organic polymers,[26−29] have been developed to improve the compatibility of Zn metal anodes with aqueous electrolytes. However, these artificial interfacial layers often suffer from uncontrollable evolution of composition and structure during battery cycling,[30,31] which potentially leads to the loss of their protective effect. Therefore, it is challenging to construct a full-featured artificial protection interphase that simultaneously possesses prominent electrochemical stability and high Zn^{2+} conductivity to suppress Zn dendrite growth and prolong cycling lifespans.

Received: September 12, 2025
Revised: November 13, 2025
Accepted: November 24, 2025
Published: November 27, 2025

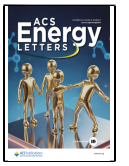

https://doi.org/10.1021/acsenergylett.5c02939
ACS Energy Lett. 2025, 10, 6489−6499

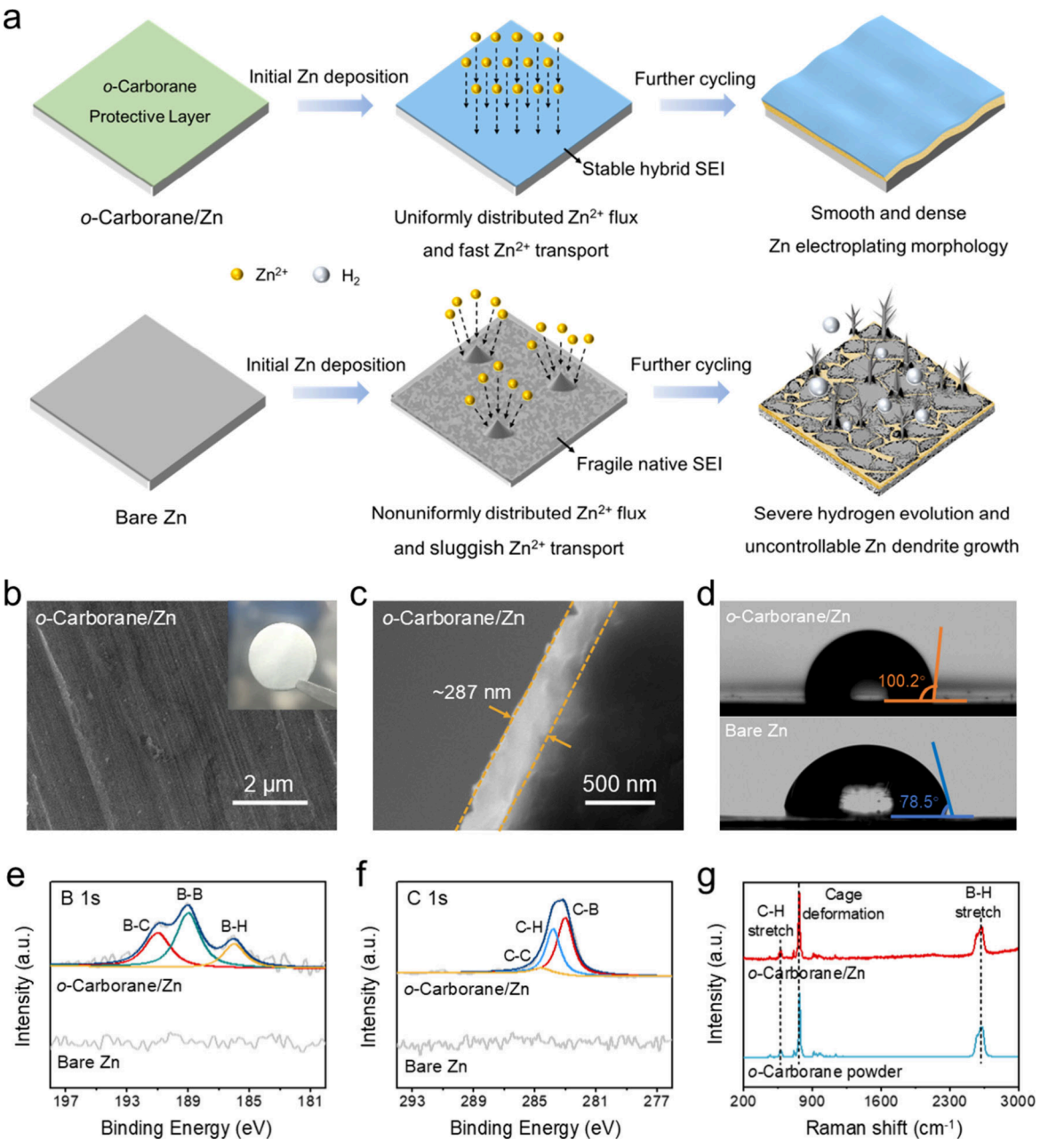

Figure 1. Compositional characterizations and protection mechanism of the *o*-carborane protection layer on Zn electrodes. (a) Schematic illustration of Zn plating/stripping processes on *o*-carborane/Zn and bare Zn electrodes. (b) Top-view SEM image and optical image (the inset) of the *o*-carborane/Zn electrode. (c) Cross-section SEM image of the *o*-carborane/Zn electrode. (d) Contact angles of 2.0 M $ZnSO_4$ aqueous solution on *o*-carborane/Zn and bare Zn electrodes. (e, f) High-resolution XPS spectra at (e) B 1s and (f) C 1s regions of *o*-carborane/Zn and bare Zn electrodes. (g) Raman spectra of the *o*-carborane/Zn electrode and pristine *o*-carborane powder.

Herein, we report the spontaneous construction of an adsorption-induced *o*-carborane artificial interphase on a Zn metal surface via the strong electrostatic attraction between cage-structured *o*-carborane clusters and Zn metal. The structural stability and chemical inertness of cage-like *o*-carborane clusters can endow Zn metal electrodes with high electrochemical durability to suppress Zn corrosion and the hydrogen evolution reaction (HER). The self-absorbed *o*-carborane clusters are demonstrated to be involved in the formation of a modified SEI. The as-formed SEI exhibits superior electrochemical stability and high Zn^{2+} conductivity, enabling improved Zn deposition morphology and exceptional long-term cycling stability of Zn metal anodes. Benefiting from the uniform anchoring of *o*-carborane clusters, the constructed artificial protection layer can effectively homogenize the surface electric field distribution and eliminate the tip effect during the initial Zn plating process, thereby inhibiting the growth of Zn dendrites. As a result, the Zn||Zn symmetric batteries assembled with *o*-carborane-modified Zn electrodes achieved a highly stable Zn plating/stripping process for over 500 h at a high current density of 10.0 mA cm^{-2}. The superior long-term cycling stability and reversibility for over 2000 cycles were also demonstrated by the Zn||Cu half-battery operated at 10.0 mA cm^{-2}. When paired with V_2O_5 cathodes, the *o*-carborane-modified Zn anodes can enable Zn||V_2O_5 batteries to work stably for over 3000 cycles at 10.0 A g^{-1}, with a

https://doi.org/10.1021/acsenergylett.5c02939
ACS Energy Lett. 2025, 10, 6489−6499

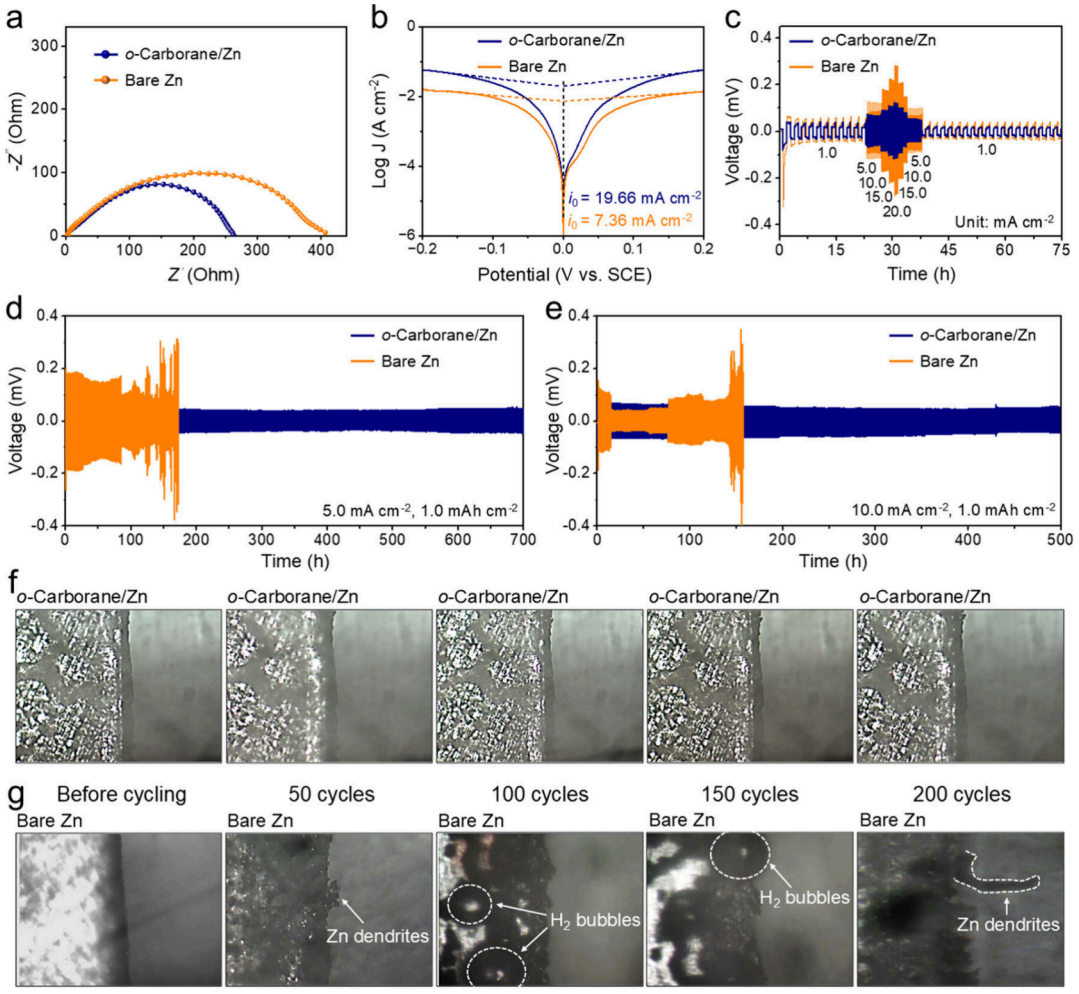

Figure 2. Electrochemical performances of Zn||Zn symmetric batteries assembled with *o*-carborane/Zn or bare Zn electrodes. (a) EIS measurements of Zn||Zn symmetric batteries. (b) Tafel plots of Zn||Zn symmetric batteries for calculating exchange current densities. (c) Rate performances of Zn||Zn symmetric batteries measured at different current densities from 1.0 to 20.0 mA cm^{-2} with a fixed capacity of 1.0 mAh cm^{-2}. (d, e) Galvanostatic cycling performances of Zn||Zn symmetric batteries (d) measured at 5.0 mA cm^{-2} with a capacity of 1.0 mAh cm^{-2} and (e) measured at 10.0 mA cm^{-2} with a capacity of 1.0 mAh cm^{-2}. (f, g) *Operando* optical microscopy observation of Zn electroplating morphology on (f) *o*-carborane/Zn and (g) bare Zn electrodes at a current density of 5.0 mA cm^{-2} for 200 cycles.

considerable remaining capacity of 145.2 mAh g^{-1}. This work provides a new perspective for constructing advanced artificial interfacial layers based on closo-type atomic clusters to propel the exploration of high-performance aqueous rechargeable multivalent-ion batteries.

The molecular structure of *o*-carborane was confirmed by Fourier transform infrared (FTIR) spectroscopic analysis (Figure S1). In this work, we employed a convenient solution immersion method to prepare the *o*-carborane cluster modified Zn metal (*o*-carborane/Zn) electrodes (Figure 1a). Briefly, by immersing the polished Zn foils into a tetrahydrofuran solution of *o*-carborane molecules (1.5 M), *o*-carborane clusters tended to spontaneously adsorb onto the Zn metal surface owing to electrostatic interactions, forming a uniform interfacial protective layer. To deeply understand the self-adsorbed behavior of *o*-carborane molecules on the Zn electrode surface, relevant theoretical calculations were performed (Figure S2). Based on molecular electrostatic potential (ESP) calculation, it could be found that the hydrogen atoms bonded to carbon atoms in *o*-carborane molecules demonstrated a more pronounced electropositive character. This illustrated the presence of potential electrostatic interactions between these C−H bonds and the Zn metal surface. Furthermore, Mulliken charge analysis quantitatively confirmed higher partial positive charges on these specific hydrogen atoms, corroborating their role as active binding sites for interaction with the Zn metal. The theoretical calculation results indicated that this spontaneous adsorption phenomenon originated from the unique molecular structure of *o*-carborane. Due to the higher electronegativity of carbon (2.55) compared to boron (2.04), the hydrogen atoms bonded to carbon atoms in *o*-carborane molecules exhibit a certain degree of Lewis acidity, which drives the molecules to strongly anchor onto the Zn metal surface, particularly at protrusions with more charge accumulation. Consequently, the self-adsorbed *o*-carborane molecules can effectively guide uniform Zn deposition, leading to a stable, dendrite-free Zn plating process.

Furthermore, the chemical inertness of cage-like *o*-carborane molecules was also investigated by theoretical calculations. According to frontier molecular orbital theory, the electrochemical stability of an SEI component is governed by its energy levels of lowest unoccupied molecular orbital (LUMO) and highest occupied molecular orbital (HOMO).[32,33] Generally, an ideal SEI component should possess a high

https://doi.org/10.1021/acsenergylett.5c02939
ACS Energy Lett. 2025, 10, 6489−6499

LUMO energy and a low HOMO energy, corresponding to a wide HOMO−LUMO gap, to ensure its high electrochemical stability. In view of this, we compared the LUMO and HOMO energies of the *o*-carborane molecule with those of conventional SEI components formed on the Zn metal electrodes (Figure S3). The *o*-carborane molecule demonstrated a high LUMO energy of −0.25 eV and a low HOMO energy of −8.58 eV. Compared with the conventional SEI components of ZnO, $Zn(OH)_2$, ZnF_2, and $Zn_4(OH)_6SO_4$, the *o*-carborane molecule possessed the highest HOMO−LUMO gap, strongly demonstrating the superior chemical stability of the *o*-carborane molecule for serving as a desirable SEI component to stabilize Zn metal. Based on the theoretical calculation results, the constructed *o*-carborane protective layer is expected to maintain high electrochemical stability throughout the prolonged cycling due to the structural stability and chemical inertness of cage-like *o*-carborane molecules, effectively suppressing Zn dendrite growth and HER of Zn metal electrodes. Notably, since *o*-carborane clusters are hydrophobic and insoluble in water (Figure S4), the as-formed *o*-carborane protective layer will not fail due to dissolution during battery assembly and operation. Different from bare Zn electrodes with metallic luster, the as-prepared *o*-carborane/Zn electrodes displayed a distinct white surface (Figure 1b), suggesting the full coverage of *o*-carborane protective layers. Scanning electron microscopy (SEM) was used to further distinguish the surface morphology of *o*-carborane/Zn and bare Zn electrodes. Compared with the bare Zn electrodes (Figure S5), *o*-carborane/Zn electrodes displayed a smoother and flatter surface morphology (Figure 1b), indicating that *o*-carborane/Zn electrodes were expected to achieve more uniform Zn nucleation. Moreover, the elemental mappings of *o*-carborane/Zn electrodes obtained through energy dispersive X-ray spectroscopy (EDX) analysis also showed the uniform distribution of Zn, B, and C elements (Figure S6). The thickness of the interfacial protective layer, as a key indicator, not only determines its physicochemical properties, but also significantly affects its protective effect.[34] In view of this, the cross-sectional morphology of *o*-carborane/Zn electrodes was further characterized via SEM investigation. As displayed in Figure 1c, the uniform and dense structural features of the *o*-carborane protective layer were detected from the side view, and the thickness of the prepared *o*-carborane protective layer was measured to be ∼287 nm on average.

The contact angle measurements of the 2.0 M aqueous $ZnSO_4$ electrolyte on the *o*-carborane/Zn and bare Zn electrodes were carried out to reveal the hydrophobic property of self-adsorbed *o*-carborane cluster protective layers (Figure 1d). Compared with the bare Zn electrode (78.5°), the contact angle of the aqueous $ZnSO_4$ electrolyte on the *o*-carborane/Zn electrode was increased to 100.2°, indicating the potential of *o*-carborane protective layers in blocking H_2O penetration and thereby suppressing the Zn corrosion and HER. The surface chemical compositions of the *o*-carborane/Zn electrode were probed by X-ray photoelectron spectroscopy (XPS). The B 1s XPS spectrum of the *o*-carborane/Zn electrode clearly exhibited the characteristic peaks of B−C, B−B, and B−H species (Figure 1e), and the characteristic peaks in the C 1s XPS spectrum were assigned to C−C, C−H, and C−B species (Figure 1f), verifying the successful modification of *o*-carborane molecules on the Zn metal surface. For the Zn 2p XPS spectra (Figure S7), no distinct peak displacement was detected before and after coating the *o*-carborane protective layer, illustrating that the construction of the *o*-carborane protective layer was based on electrostatic adsorption rather than chemical reaction. The Raman spectrum of the *o*-carborane/Zn electrode was also measured to further confirm its surface chemical compositions. As displayed in Figure 1g, three typical characteristic peaks, corresponding to the C−H stretching, cage deformation, and B−H stretching of *o*-carborane molecules, were detected on the surface of *o*-carborane/Zn electrodes, indicating the spontaneous formation of the self-adsorbed *o*-carborane protection layer.

To demonstrate the improved electrochemical kinetics and cycling stability of the *o*-carborane/Zn electrodes, the Zn||Zn symmetric batteries were assembled with *o*-carborane/Zn or bare Zn electrodes. Electrochemical impedance spectroscopy (EIS) measurements showed a markedly decreased interfacial impedance of the *o*-carborane/Zn electrode than that of a bare Zn electrode (Figure 2a), illustrating that the constructed *o*-carborane protective layer could efficiently enhance interfacial charge transfer kinetics.[35] The EIS measurements of Zn||Zn symmetric batteries after various cycles were also conducted (Figure S10). The Zn||Zn symmetric batteries with *o*-carborane/Zn electrodes consistently maintained lower interfacial impedances than those with bare Zn electrodes after different cycles. This fully confirms that the *o*-carborane protective layer can efficiently accelerate the Zn^{2+} transport kinetics and provide long-term protection for the Zn metal electrodes. This conclusion was further verified by the exchange current densities (i_0) calculated based on the Tafel plots of Zn||Zn symmetric batteries. As shown in Figure 2b, the i_0 value of the *o*-carborane/Zn electrode was measured to be 19.66 mA cm^{-2}, much higher than that of the bare Zn electrode (7.36 mA cm^{-2}), indicating faster Zn^{2+} transport at the interface between the *o*-carborane/Zn electrode and the electrolyte.[36] Furthermore, apparent activation energies (E_a) for Zn^{2+} diffusion through the different SEIs were calculated by linearly fitting $\ln(T/R_{SEI})$ versus $1/T$ (Figure S11). For the *o*-carborane/Zn electrodes, the E_a value was 20.74 kJ mol^{-1} (Figure S12), whereas it was up to 25.03 kJ mol^{-1} when using the bare Zn electrodes, confirming the favorable mass-transfer kinetics of the constructed *o*-carborane protective layer. The rate capabilities of Zn||Zn symmetric batteries were investigated at various current densities from 1.0 to 20.0 mA cm^{-2} (Figure 2c). The Zn||Zn symmetric batteries based on *o*-carborane/Zn electrodes exhibited flat and regular voltage platforms, even at high current densities. The overpotentials were around 25, 65, 88, 106, and 123 mV at current densities of 1.0, 5.0, 10.0, 15.0, and 20.0 mA cm^{-2}, respectively. In contrast, For the Zn||Zn symmetric batteries based on bare Zn electrodes, the voltage hysteresis sharply increased from 33 to 276 mV with the increase of current densities from 1.0 to 20.0 mA cm^{-2}, indicating that it was difficult for bare Zn electrodes to achieve high-efficient Zn^{2+} transfer at such high current densities.

The long-term cycling performances of Zn||Zn symmetric batteries assembled with different electrodes were tested to further evaluate the reliability of the *o*-carborane protective layer. At a low current density of 1.0 mA cm^{-2} with a capacity of 1.0 mAh cm^{-2} (Figure S13), the Zn||Zn symmetric batteries with *o*-carborane/Zn electrodes achieved a stable Zn plating/stripping process for over 590 h, while the Zn||Zn symmetric batteries with bare Zn electrodes exhibited a clear increase in voltage polarization and were close to failure after 200 h. When cycled at 5.0 mA cm^{-2} with a capacity of 1.0 mAh cm^{-2}

https://doi.org/10.1021/acsenergylett.5c02939
ACS Energy Lett. 2025, 10, 6489−6499

(Figure 2d), the Zn||Zn symmetric batteries based on *o*-carborane/Zn electrodes displayed outstanding cycling stability for over 700 h with an ultralow overpotential of ~48 mV, demonstrating boosted interfacial stability and accelerated reaction kinetics. In sharp contrast, the Zn||Zn symmetric batteries based on bare Zn electrodes could only cycle stably for less than 86 h and then showed remarkable fluctuations of voltage curves, illustrating that the bare Zn electrodes suffered from severe electrolyte corrosion and uncontrollable Zn dendrite growth. At a higher current density of 10.0 mA cm^{-2}, the Zn||Zn symmetric batteries based on *o*-carborane/Zn electrodes showed steady Zn plating/stripping behaviors for over 500 h with limited voltage polarization, fully confirming the crucial role of the *o*-carborane protective layer in stabilizing Zn metal electrodes. By comparison, the Zn||Zn symmetric batteries based on bare Zn electrodes encountered a sharp decrease in voltage hysteresis after cycling for only 14 h (Figure 2e), indicating the fragile native SEI could not provide long-term protection for bare Zn electrodes at high current densities. To further demonstrate the improvement effect of the *o*-carborane protective layer on Zn plating/stripping kinetics, the detailed voltage curves of *o*-carborane/Zn and bare Zn electrodes were compared (Figure S14). At the current densities of 5.0 mA cm^{-2} and 10.0 mA cm^{-2}, the Zn||Zn symmetric batteries based on *o*-carborane/Zn electrodes exhibited smaller voltage polarization, demonstrating the better reaction kinetics of the *o*-carborane/Zn electrodes. The galvanostatic intermittent titration technique (GITT) curves of the *o*-carborane/Zn and bare Zn electrodes were also measured. As shown in Figure S15, the concentration polarization decreased from 9.2 to 4.3 mV after the modification of the *o*-carborane protective layer on bare Zn electrodes. Besides, the ohmic-interfacial polarization of *o*-carborane/Zn electrodes also decreased to 40.7 mV compared with bare Zn electrodes (67.9 mV), indicating improved desolvation kinetics and faster Zn^{2+} migration in the SEI of *o*-carborane/Zn electrodes. The electrochemical performances of Zn||Zn symmetric batteries assembled with *o*-carborane/Zn electrodes were compared with those of previously reported Zn electrodes stabilized by different artificial SEI layers (Table S1),[30,37−45] further highlighting the superiority of the as-built *o*-carborane protective layer in stabilizing Zn metal electrodes.

To intuitively reveal the differences of *o*-carborane/Zn and bare Zn electrodes in Zn electroplating morphology evolution, *in situ* optical microscopy observations were conducted to monitor the Zn plating/stripping process in real time. For the *o*-carborane/Zn electrodes, stable Zn plating/stripping behaviors were well maintained throughout the cycling process (Figure 2f). The surface of the *o*-carborane/Zn electrodes displayed a smooth and dense morphology without any visible Zn dendrites and H_2 bubbles after 200 cycles, confirming that the constructed *o*-carborane protective layer could effectively enhance interfacial stability, suppress undesirable Zn corrosion and HER, and facilitate uniform Zn electrodeposition. In sharp contrast, for the bare Zn electrodes, a rough electrode surface covered by mossy-like Zn dendrites was observed after only 50 cycles (Figure 2g). As the Zn plating/stripping process continued, the uneven Zn deposition was further aggravated, and H_2 bubbles originating from the HER were also observed on the bare Zn surface. Finally, the surface of bare Zn electrodes was fully covered by numerous Zn dendrites.

To highlight the superior chemical stability of the *o*-carborane protective layer, the *o*-carborane/Zn and bare Zn electrodes were directly immersed in a 2.0 M aqueous $ZnSO_4$ electrolyte for 1 week to observe the changes on the electrode surfaces. As shown in Figure 3a, the *o*-carborane/Zn electrode

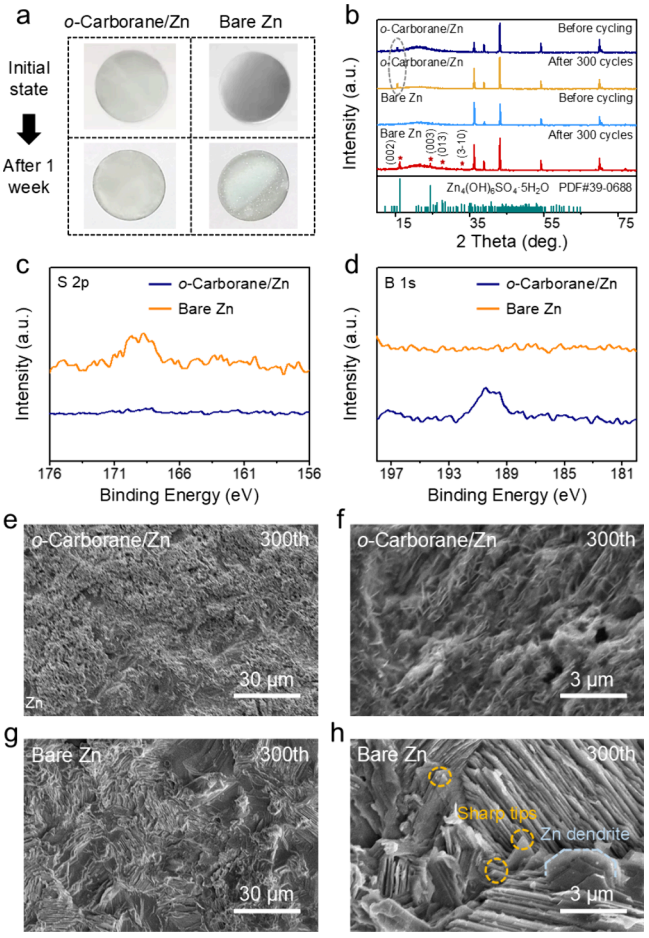

Figure 3. Surface compositions and morphology characterizations of the cycled *o*-carborane/Zn and bare Zn electrodes. (a) Optical images of *o*-carborane/Zn and bare Zn electrodes at the initial state and after immersing in a 2.0 M aqueous $ZnSO_4$ electrolyte for 1 week. (b) XRD patterns of *o*-carborane/Zn and bare Zn electrodes before and after 300 cycles. (c, d) High-resolution XPS spectra at (c) S 2p and (d) B 1s regions of *o*-carborane/Zn and bare Zn electrodes retrieved from Zn||Zn symmetric batteries after 300 cycles. (e−h) Top-view SEM images of (e, f) *o*-carborane/Zn and (g, h) bare Zn electrodes retrieved from Zn||Zn symmetric batteries after 300 cycles.

exhibited a well-maintained original morphology, demonstrating its impressive chemical stability in the aqueous electrolyte. In contrast, the bare Zn electrode visibly rusted and lost its metallic luster due to the serious corrosion reaction of Zn metal in an aqueous $ZnSO_4$ electrolyte. Moreover, the Zn||Zn symmetric batteries based on *o*-carborane/Zn electrodes after immersing in a 2.0 M aqueous $ZnSO_4$ electrolyte for 1 week also demonstrated a markedly prolonged cycling lifespan (Figure S16), verifying the effectiveness of the *o*-carborane protective layer in boosting the interfacial stability of Zn metal electrodes. Systematical spectroscopic characterizations further confirmed the protective effect of the *o*-carborane protective layer. The X-ray diffraction (XRD) patterns of the *o*-carborane/Zn electrode (Figure 3b) showed no obvious signal peaks of $Zn_4(OH)_6SO_4{\cdot}5H_2O$ or other byproducts after 300

https://doi.org/10.1021/acsenergylett.5c02939
ACS Energy Lett. 2025, 10, 6489−6499

cycles, confirming the critical role of the *o*-carborane protective layer in protecting Zn metal from electrolyte attack. It is worth noting that the characteristic peaks corresponding to *o*-carborane could be detected identically before and after 300 cycles (Figure S8), illustrating that the constructed *o*-carborane protective layer could be tightly anchored to the Zn metal surface to provide long-term protection for the Zn metal electrodes. By comparison, the XRD patterns of the bare Zn electrode exhibited several strong characteristic peaks assigned to $Zn_4(OH)_6SO_4{\cdot}5H_2O$ byproducts after 300 cycles, indicating that the bare Zn surface suffered from severe electrolyte corrosion.[46,47] To clarify the structural differences of the SEIs formed on the *o*-carborane/Zn and bare Zn electrodes, transmission electron microscopy (TEM) characterizations were employed. For the *o*-carborane/Zn electrodes (Figure S17a), the as-formed SEI exhibited a uniform thickness of approximately 19.8 nm and was almost entirely composed of short-range-ordered microcrystals. Combined with the XRD results, it could be inferred that this SEI consisted of numerous microcrystals formed by *o*-carborane molecules. The uniform and compact structure of this SEI effectively prevented the corrosion of Zn metal by electrolytes, thereby suppressing the formation of byproducts such as $Zn_4(OH)_6SO_4$, ZnO, and $Zn(OH)_2$. In contrast, the SEI on the bare Zn electrodes exhibits a highly nonuniform thickness and a typical mosaic-like structure (Figure S17b). The magnified TEM image revealed that the SEI on the bare Zn electrodes primarily consisted of $Zn_4(OH)_6SO_4$, ZnO, and $Zn(OH)_2$ species along with some amorphous phases. This type of SEI failed to protect the active zinc metal from electrolyte corrosion, consequently triggering zinc dendrite growth and severe HER.

The differences in surface chemical compositions of the cycled *o*-carborane/Zn and bare Zn electrodes were further investigated by XPS analysis. In the S 2p spectra (Figure 3c), a distinct signal response was detected on the bare Zn surface, indicating that the decomposition of the $ZnSO_4$ electrolyte resulted in the generation of sulfur-containing species on the bare Zn surface. In the B 1s spectra (Figure 3d), the characteristic peak assigned to *o*-carborane was still detected on the *o*-carborane/Zn surface after 300 cycles, further verifying its impressive interfacial stability. To verify the effectiveness of the as-formed *o*-carborane protective layer in inhibiting Zn dendrite growth, the surface morphologies of *o*-carborane/Zn and bare Zn electrodes after 300 cycles were systematically investigated by the SEM technique. The *o*-carborane/Zn electrode showed a homogeneous and dense surface morphology without visible Zn dendrites (Figure 3e,f). It is evident that the constructed *o*-carborane protective layer could efficiently improve the uniformity of Zn deposition and provide long-term protection for Zn metal electrodes to avoid electrolyte attack. In contrast, the cycled bare Zn electrode presented a rugged and uneven surface (Figure 3g). The further magnified SEM image clearly showed that the bare Zn electrode was completely covered with Zn dendrites with sharp tips (Figure 3h).

To demonstrate the superiority of the *o*-carborane protective layer in enhancing Zn plating/stripping reversibility, the electrochemical performances of Zn||Cu half-batteries based on *o*-carborane-modified Cu (*o*-carborane/Cu) or bare Cu electrodes were measured (Figure S9). Cyclic voltammetry (CV) measurements of Zn||Cu half-batteries were first performed within the voltage range of −0.3 to 0.8 V. Compared with the Zn||Cu half-batteries with bare Cu electrodes, the current responses of the Zn||Cu half-batteries based on *o*-carborane/Cu electrodes increased markedly during the initial Zn plating/stripping process (Figure 4a),

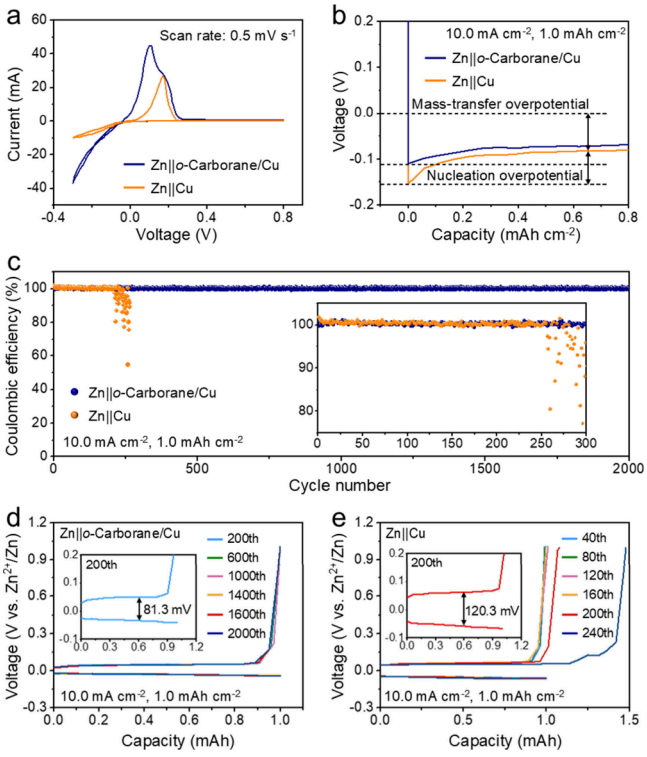

Figure 4. Electrochemical performances of Zn||Cu half-batteries assembled with *o*-carborane/Cu or bare Cu electrodes. (a) CV curves of Zn||Cu half-batteries at a scan rate of 5.0 mV s^{-1} from −0.3 to 0.8 V. (b) Comparison of initial Zn plating profiles for Zu|| Cu half-batteries with *o*-carborane/Cu or bare Cu electrodes measured at 10.0 mA cm^{-2} with a capacity of 1.0 mAh cm^{-2}. (c) CE tests of Zn||Cu half-batteries at 10.0 mA cm^{-2} with a capacity of 1.0 mAh cm^{-2}. (d, e) Galvanostatic voltage profiles at different cycles of (d) Zn||*o*-carborane/Cu and (e) Zn||Cu half-batteries measured at 10.0 mA cm^{-2} with a capacity of 1.0 mAh cm^{-2}.

corresponding to rapid Zn^{2+} transport and reversible reaction kinetics.[48] The difference in the initial Zn deposition overpotential was investigated by monitoring the initial Zn plating profiles of Zn||Cu half-batteries (Figure 4b). When using the *o*-carborane/Cu electrodes, the mass-transfer and nucleation overpotentials of batteries were 72.0 and 38.2 mV, respectively, at 10.0 mA cm^{-2} (Figure S19), both of which were lower than those of Zn||Cu half-batteries based on bare Cu electrodes (82.8 and 71.3 mV), revealing that the *o*-carborane protective layer could efficiently accelerate Zn^{2+} transfer and reduce the energy barrier of Zn nucleation. The same conclusion could also be drawn by analyzing the initial Zn plating profiles at current densities of 1.0 mA cm^{-2} and 5.0 mA cm^{-2} (Figure S18). The Zn||*o*-carborane/Cu batteries consistently maintained overpotentials for both mass-transfer and nucleation processes lower than those of Zn||bare Cu batteries (Figure S19). This confirmed that the *o*-carborane protective layer could effectively improve mass-transfer kinetics and reduce the energy barrier of the initial Zn nucleation.

The long-term Zn plating/stripping tests of Zn||Cu half-batteries were conducted to check the cycling reversibility of the *o*-carborane/Cu electrodes (Figure 4c). At 10.0 mA cm^{-2},

https://doi.org/10.1021/acsenergylett.5c02939
ACS Energy Lett. 2025, 10, 6489−6499

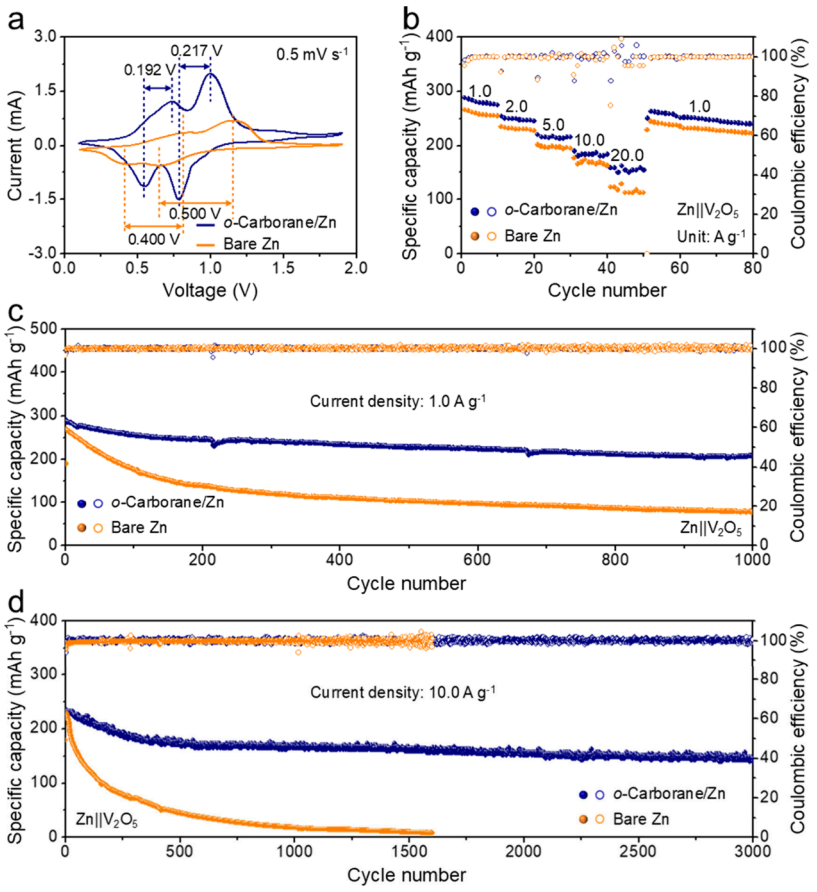

Figure 5. Electrochemical performances of Zn||V_2O_5 batteries assembled with *o*-carborane/Zn or bare Zn anodes. (a) Comparison of CV curves for Zn||V_2O_5 batteries at a scan rate of 0.5 mV s^{-1} from 0.1 to 1.8 V. (b) Rate performances of Zn||V_2O_5 batteries measured at different current densities from 1.0 to 20.0 A g^{-1}. (c, d) Long-term cycling performances of Zn||V_2O_5 batteries measured at (c) 1.0 and (d) 10.0 A g^{-1}.

the Zn||Cu half-batteries based on *o*-carborane/Cu electrodes displayed superior Zn plating/stripping stability for 2000 cycles, delivering an average Coulombic efficiency (CE) of above 99.5%. In contrast, a marked CE fluctuation was observed for the batteries based on bare Cu electrodes after less than 200 cycles, indicating a rapid battery failure. The significant differences of *o*-carborane/Cu and bare Cu electrodes in Zn plating/stripping reversibility could be partially ascribed to the key role of the *o*-carborane protective layer in facilitating Zn^{2+} transport, which was also verified by the voltage polarization presented by galvanostatic voltage profiles at different cycles. Compared with the bare Cu electrode, the *o*-carborane/Cu electrode displayed ultrahigh Zn utilization and nearly overlapped voltage curves with lower overpotentials even after 2000 cycles (Figure 4d). By further comparing the voltage polarization at the 200th cycle (Figure 4e), the *o*-carborane/Cu electrode exhibited a lower overpotential of 81.3 mV than that of the bare Cu electrode (120.3 mV), indicating that the *o*-carborane protective layer played a key role in boosting the electrochemical kinetic performance.[36] Moreover, the morphology differences of Zn electroplating behaviors on *o*-carborane/Cu and bare Cu electrodes were also investigated by SEM. As shown in Figure S20, the deposited Zn metal on the *o*-carborane/Cu electrode exhibited a uniform and relatively flat surface morphology without remarkable Zn particle aggregation (Figure S20a–c). The cross-section SEM images of as-deposited Zn metal on the *o*-carborane/Cu electrode also demonstrated dense and dendrite-free Zn deposition behaviors, and the thickness of the Zn plating layer was homogeneous (Figure S20d–f). By comparison, the deposited Zn metal on a bare Cu electrode displayed serious Zn particle aggregation due to nonuniform Zn deposition (Figure S20g–i), and the rough and loose morphology of Zn deposition was observed clearly from the side view (Figure S20j–l).

To further verify the practicality of *o*-carborane/Zn protective layers, Zn||V_2O_5 batteries assembled with *o*-carborane/Zn and bare Zn anodes were systematically tested. Prior to battery assembly, the V_2O_5 cathode material was subjected to a Zn^{2+} preintercalation pretreatment to enhance its Zn^{2+} intercalation/deintercalation capability. The morphology and structure of the Zn^{2+}-intercalated V_2O_5 cathode were characterized by SEM and XRD analyses (Figures S21 and S22). The CV curves of Zn||V_2O_5 batteries at different cycles were measured at 0.5 mV s^{-1} within the voltage range of 0.1–1.9 V. As shown in Figure S23, the Zn||V_2O_5 batteries assembled with both *o*-carborane/Zn or bare Zn anodes exhibited two pairs of redox peaks, corresponding to the redox pairs of V^{5+}/V^{4+} and V^{4+}/V^{3+}, respectively. Compared with the bare Zn||V_2O_5 batteries, the CV curves of *o*-carborane/Zn||V_2O_5 batteries were nearly overlapped and exhibited higher redox current responses, indicating better reaction kinetics.[49] Moreover, it was revealed by further comparing the CV curves of the fifth cycle that the *o*-carborane/Zn||V_2O_5 batteries

https://doi.org/10.1021/acsenergylett.5c02939
ACS Energy Lett. 2025, 10, 6489–6499

achieved smaller voltage difference for the redox pairs of V^{5+}/V^{4+} (0.217 V) and V^{4+}/V^{3+} (0.192 V) (Figure 5a), indicating the improved redox kinetics.[50] The rate performances of Zn||V_2O_5 batteries assembled with *o*-carborane/Zn or bare Zn anodes were measured at different current densities from 1.0 to 20.0 A g^{-1} (Figure 5b). The Zn||V_2O_5 batteries assembled with *o*-carborane/Zn anodes exhibited an improved rate capability, delivering reversible discharge capacities of 280.7, 249.0, 215.9, 183.9, and 154.4 mAh g^{-1} at 1.0, 5.0, 10.0, 15.0, and 20.0 A g^{-1}, respectively. In contrast, for the Zn||V_2O_5 batteries assembled with bare Zn anodes, the specific discharge capacities decreased markedly with the increase in current densities, indicating the sluggish reaction kinetics of bare Zn anodes. Notably, the Zn||V_2O_5 batteries with bare Zn anodes exhibited more pronounced fluctuations at 20 A g^{-1} in both discharge capacity and CE compared with the batteries with *o*-carborane-modified Zn anodes. This indicated that the bare Zn anodes underwent uncontrollable dendrite growth, intensified hydrogen evolution, and severe interfacial passivation under such a high current density. In contrast, the construction of *o*-carborane protective layers was conducive to mitigating such electrode/electrolyte interfacial instability, verifying the effectiveness of *o*-carborane modification. The superior rate performance of *o*-carborane/Zn anodes was attributed to the lower voltage polarization and better reaction kinetics, which were further confirmed by smaller potential differences between charge/discharge plateaus at various current densities of *o*-carborane/Zn anodes (Figure S24).

The long-term cycling performances of Zn||V_2O_5 batteries based on *o*-carborane/Zn or bare Zn anodes were evaluated at different current densities. When using the *o*-carborane/Zn anodes, the Zn||V_2O_5 batteries demonstrated the markedly enhanced cycling stability at 1.0 A g^{-1}, delivering a considerable remaining capacity of 207.5 mAh g^{-1} after 1000 cycles, corresponding to a capacity retention of 71.5%. In contrast, the Zn||V_2O_5 batteries based on bare Zn anodes exhibited significant capacity degradation (Figure 5c). After 1000 cycles, the specific discharge capacity of bare Zn||V_2O_5 batteries was only 21.4 mAh g^{-1}. When the current density was increased to 10.0 A g^{-1} (Figure 5d), the Zn||V_2O_5 batteries assembled with *o*-carborane/Zn anodes exhibited significantly improved cycling stability, delivering a high remaining capacity of 145.2 mAh g^{-1} even after 3000 cycles. In comparison, the Zn||V_2O_5 batteries based on bare Zn anodes suffered from severe capacity decay and remarkable CE fluctuation, and the specific discharge capacity of batteries rapidly decayed to 7.7 mAh g^{-1} after 1600 cycles. Impressively, the exceptional cycling stability of *o*-carborane/Zn||V_2O_5 batteries is highly competitive compared to previously reported Zn||V_2O_5 batteries assembled with interface-modified Zn metal anodes (Table S2).[30,37,51−58] To further examine the practical reliability of *o*-carborane/Zn anodes, the *o*-carborane/Zn||V_2O_5 batteries assembled with high-loading V_2O_5 cathodes (4.83, 5.67, and 7.41 mg cm^{-2}) were tested (Figure S25). The *o*-carborane/Zn||V_2O_5 batteries with a high mass loading of active materials could work stably for long-term cycles, highlighting the crucial role of the *o*-carborane protective layer in improving interfacial stability.

In summary, we report a promising strategy to spontaneously construct an *o*-carborane cluster-based artificial interfacial layer on the Zn metal surface. The self-absorbed *o*-carborane clusters were able to optimize the chemical compositions of SEI on the Zn metal surface. The as-formed *o*-carborane-rich SEI could effectively protect fresh Zn metal from aqueous electrolyte attack and markedly accelerate Zn^{2+} transfer, thus achieving a highly stable and reversible Zn plating/stripping process. Benefiting from their superior structural stability and chemical inertness, the self-anchored *o*-carborane clusters efficiently enhanced electrochemical durability of Zn metal anodes, thereby inhibiting undesirable Zn corrosion and the HER. Systematic electrochemical analyses and measurements demonstrated that the as-constructed *o*-carborane protective layer could effectively redistribute Zn^{2+} flux and promote uniform Zn electrodeposition, thus inhibiting the proliferation of Zn dendrites. Consequently, the assembled Zn||Zn symmetric batteries and Zn||Cu half-batteries demonstrated markedly prolonged cycling lifespans and improved Zn plating/stripping reversibility at a high current density of 10.0 mA cm^{-2}. When paired with V_2O_5 cathodes, the *o*-carborane/Zn anodes also exhibited exceptional cycling performance, enabling Zn||V_2O_5 batteries to achieve low voltage polarization, outstanding rate performance, and considerable capacity retention. This work provides new insights into the design of advanced artificial protective layers based on closo-type atomic clusters for stabilizing transition metal anodes, presenting a promising route to develop aqueous multivalent-ion batteries aimed at high-safety and low-cost energy storage applications.

■ ASSOCIATED CONTENT

Data Availability Statement

The data that support the findings of this study are available from the corresponding author upon reasonable request.

Supporting Information

The Supporting Information is available free of charge at https://pubs.acs.org/doi/10.1021/acsenergylett.5c02939.

Experimental section (including material preparation, material characterizations, electrochemical measurements, and theoretical calculations), additional figures (Figure S1−S25), additional tables (Tables S1 and S2) (PDF)

■ AUTHOR INFORMATION

Corresponding Author

Zhong Jin − *State Key Laboratory of Coordination Chemistry, MOE Key Laboratory of Mesoscopic Chemistry, MOE Key Laboratory of High Performance Polymer Materials and Technology, Jiangsu Key Laboratory of Clean Energy Catalysis and Intelligent Green Chemical Engineering, Suzhou Key Laboratory of Green Intelligent Manufacturing of New Energy Materials and Devices, Tianchang New Materials and Energy Technologies Research Center, Institute of Green Chemistry and Engineering, School of Chemistry and Chemical Engineering, Nanjing University, Nanjing, Jiangsu 210023, P. R. China;* orcid.org/0000-0001-8860-8579; Email: zhongjin@nju.edu.cn

Authors

Yuge Feng − *School of Electronic Science and Engineering, Southeast University, Nanjing, Jiangsu 210096, China; State Key Laboratory of Coordination Chemistry, MOE Key Laboratory of Mesoscopic Chemistry, MOE Key Laboratory of High Performance Polymer Materials and Technology, Jiangsu Key Laboratory of Clean Energy Catalysis and Intelligent Green Chemical Engineering, Suzhou Key*

Laboratory of Green Intelligent Manufacturing of New Energy Materials and Devices, Tianchang New Materials and Energy Technologies Research Center, Institute of Green Chemistry and Engineering, School of Chemistry and Chemical Engineering, Nanjing University, Nanjing, Jiangsu 210023, P. R. China

Yaoda Wang − *State Key Laboratory of Coordination Chemistry, MOE Key Laboratory of Mesoscopic Chemistry, MOE Key Laboratory of High Performance Polymer Materials and Technology, Jiangsu Key Laboratory of Clean Energy Catalysis and Intelligent Green Chemical Engineering, Suzhou Key Laboratory of Green Intelligent Manufacturing of New Energy Materials and Devices, Tianchang New Materials and Energy Technologies Research Center, Institute of Green Chemistry and Engineering, School of Chemistry and Chemical Engineering, Nanjing University, Nanjing, Jiangsu 210023, P. R. China*

Junchuan Liang − *State Key Laboratory of Coordination Chemistry, MOE Key Laboratory of Mesoscopic Chemistry, MOE Key Laboratory of High Performance Polymer Materials and Technology, Jiangsu Key Laboratory of Clean Energy Catalysis and Intelligent Green Chemical Engineering, Suzhou Key Laboratory of Green Intelligent Manufacturing of New Energy Materials and Devices, Tianchang New Materials and Energy Technologies Research Center, Institute of Green Chemistry and Engineering, School of Chemistry and Chemical Engineering, Nanjing University, Nanjing, Jiangsu 210023, P. R. China*

Lina Qin − *State Key Laboratory of Coordination Chemistry, MOE Key Laboratory of Mesoscopic Chemistry, MOE Key Laboratory of High Performance Polymer Materials and Technology, Jiangsu Key Laboratory of Clean Energy Catalysis and Intelligent Green Chemical Engineering, Suzhou Key Laboratory of Green Intelligent Manufacturing of New Energy Materials and Devices, Tianchang New Materials and Energy Technologies Research Center, Institute of Green Chemistry and Engineering, School of Chemistry and Chemical Engineering, Nanjing University, Nanjing, Jiangsu 210023, P. R. China*

Kaiqiang Zhang − *State Key Laboratory of Coordination Chemistry, MOE Key Laboratory of Mesoscopic Chemistry, MOE Key Laboratory of High Performance Polymer Materials and Technology, Jiangsu Key Laboratory of Clean Energy Catalysis and Intelligent Green Chemical Engineering, Suzhou Key Laboratory of Green Intelligent Manufacturing of New Energy Materials and Devices, Tianchang New Materials and Energy Technologies Research Center, Institute of Green Chemistry and Engineering, School of Chemistry and Chemical Engineering, Nanjing University, Nanjing, Jiangsu 210023, P. R. China;* orcid.org/0000-0002-2288-4893

Shuhong Xu − *School of Electronic Science and Engineering, Southeast University, Nanjing, Jiangsu 210096, China*

ChunLei Wang − *School of Electronic Science and Engineering, Southeast University, Nanjing, Jiangsu 210096, China;* orcid.org/0000-0002-7675-8921

Complete contact information is available at: https://pubs.acs.org/10.1021/acsenergylett.5c02939

Author Contributions

#Y. Feng and Y. Wang contributed equally to this work.

Notes

The authors declare no competing financial interest.

■ ACKNOWLEDGMENTS

The authors appreciate the support by the National Natural Science Foundation of China (U25A20628, 22561160129, 22479074, 22475096), the Equipment Pre-Research and Ministry of Education Joint Fund (8091B02052407), the Fundamental Research Program Key Project of Jiangsu Province (BK20253008), the Science and Technology Major Project of Jiangsu Province (BG2024013), the Scientific and Technological Achievements Transformation Special Fund of Jiangsu Province (BA2023037), the Academic Degree and Postgraduate Education Reforming Project of Jiangsu Province (JGKT24_C001), the Key Core Technology Open Competition Project of Suzhou City (SYG2024122), the Open Research Fund of Suzhou Laboratory (SZLAB-1308-2024-TS005), and the Chenzhou National Sustainable Development Agenda Innovation Demonstration Zone Provincial Special Project (2023sfq11).

■ REFERENCES

(1) Parker, J. F.; Chervin, C. N.; Pala, I. R.; Machler, M.; Burz, M. F.; Long, J. W.; Rolison, D. R. Rechargeable nickel−3D zinc batteries: an energy-dense, safer alternative to lithium-ion. *Science* **2017**, *356*, 415−418.

(2) Li, C.; Jin, S.; Archer, L. A.; Nazar, L. F. Toward practical aqueous zinc-ion batteries for electrochemical energy storage. *Joule* **2022**, *6*, 1733−1738.

(3) Yang, C.; Xia, J.; Cui, C.; Pollard, T. P.; Vatamanu, J.; Faraone, A.; Dura, J. A.; Tyagi, M.; Kattan, A.; Thimsen, E.; Xu, J.; Song, W.; Hu, E.; Ji, X.; Hou, S.; Zhang, X.; Ding, M. S.; Hwang, S.; Su, D.; Ren, Y.; Yang, X.-Q.; Wang, H.; Borodin, O.; Wang, C. All-temperature zinc batteries with high-entropy aqueous electrolyte. *Nat. Sustain.* **2023**, *6*, 325−335.

(4) Wang, F.; Borodin, O.; Gao, T.; Fan, X.; Sun, W.; Han, F.; Faraone, A.; Dura, J. A.; Xu, K.; Wang, C. Highly reversible zinc metal anode for aqueous batteries. *Nat. Mater.* **2018**, *17*, 543−549.

(5) Deng, Y.-P.; Liang, R.; Jiang, G.; Jiang, Y.; Yu, A.; Chen, Z. The current state of aqueous Zn-based rechargeable batteries. *ACS Energy Lett.* **2020**, *5*, 1665−1675.

(6) Yang, S.-J.; Zhao, L.-L.; Li, Z.-X.; Wang, P.; Liu, Z.-L.; Shu, J.; Yi, T.-F. Achieving stable Zn anode via artificial interfacial layers protection strategies toward aqueous Zn-ion batteries. *Coord. Chem. Rev.* **2024**, *517*, 216044.

(7) Liu, X.; Sun, L.; Zhao, Z.; Lu, Q. Solvation structure tuning for advanced aqueous zinc-ion batteries. *J. Energy Storage* **2024**, *89*, 111822.

(8) Thomas, T. S.; Sinha, A. P.; Mandal, D. Modulating electrolyte solvation for high performance aqueous zinc−sulfur batteries. *J. Mater. Chem. A* **2024**, *12*, 21350.

(9) Wang, H.; Wang, K.; Jing, E.; Wei, M.; Xiong, J.; Zhong, D.; Zuo, Y.; Liang, B.; Pei, P. Strategies of regulating Zn^{2+} solvation structures toward advanced aqueous zinc-based batteries. *Energy Storage Mater.* **2024**, *70*, 103451.

(10) Zhang, Q.; Ma, Y.; Lu, Y.; Ni, Y.; Lin, L.; Hao, Z.; Yan, Z.; Zhao, Q.; Chen, J. Halogenated Zn^{2+} solvation structure for reversible Zn metal batteries. *J. Am. Chem. Soc.* **2022**, *144*, 18435−18443.

(11) Wang, Y.; Li, Q.; Hong, H.; Yang, S.; Zhang, R.; Wang, X.; Jin, X.; Xiong, B.; Bai, S.; Zhi, C. Lean-water hydrogel electrolyte for zinc ion batteries. *Nature Commun.* **2023**, *14*, 3890.

(12) Sun, L.; Yao, Y.; Dai, L.; Jiao, M.; Ding, B.; Yu, Q.; Tang, J.; Liu, B. Sustainable and high-performance Zn dual-ion batteries with a hydrogel-based water-in-salt electrolyte. *Energy Storage Mater.* **2022**, *47*, 187−194.

(13) Wang, Z.; Xue, R.; Zhang, H.; Zhang, Y.; Tang, X.; Wang, H.; Shao, A.; Ma, Y. A hydrogel electrolyte toward a flexible zinc-ion

battery and multifunctional health monitoring electronics. *ACS Nano* **2024**, *18*, 7596−7609.
(14) Hu, Y.; Wang, Z.; Li, Y.; Liu, P.; Liu, X.; Liang, G.; Zhang, D.; Fan, X.; Lu, Z.; Wang, W. Sulfonated hydrogel electrolyte enables dendrite-free zinc-ion batteries. *Chem. Eng. J.* **2024**, *479*, 147762.
(15) Hu, Y.; Shen, P.; Zeng, N.; Wang, L.; Yan, D.; Cui, L.; Yang, K.; Zhai, C. Hybrid hydrogel electrolyte based on metal−organic supermolecular self-assembly and polymer chemical cross-linking for rechargeable aqueous Zn−MnO_2 batteries. *ACS Appl. Mater. Interfaces* **2020**, *12*, 42285−42293.
(16) Mamat, M.; Wu, J.; Yang, L.; Abliz, A.; Wang, S.; Li, H. Highly Stable Amorphous InGaSnO Coating for Aqueous Zn Ion Batteries with a Long Cycling Life. *ACS Sustainable Chem. Eng.* **2025**, *13*, 12553−12563.
(17) Wu, J.; Yang, L.; Zhou, S.; Wang, S.; Abliz, A.; Wu, R.; Zhu, K.; Yao, X.; Li, H.; Wang, J.; Mi, H.; Li, J.; Pan, A. Long-Lasting Zn Metal Anode Coated with an Industrially Available Amorphous InGaZnO Layer. *Chem. Eng. J.* **2024**, *501*, 157729.
(18) Wu, J.; Yang, L.; Wang, S.; Abliz, A.; Tuokedaerhan, K.; Li, H.; Li, J.; Wang, J.; Pan, A. Triple-Functional Amorphous In_2O_3 Anode Protection Layer Design for High-Performance Aqueous Zinc Ion Batteries. *Adv. Funct. Mater.* **2025**, *35*, 2419492.
(19) Xu, Y.; Zheng, X.; Sun, J.; Wang, W.; Wang, M.; Yuan, Y.; Chuai, M.; Chen, N.; Hu, H.; Chen, W. Nucleophilic interfacial layer enables stable Zn anodes for aqueous Zn batteries. *Nano Lett.* **2022**, *22*, 3298−3306.
(20) Liu, K.; Sun, M.; Yang, S.; Gan, G.; Bu, S.; Zhu, A.; Lin, D.; Zhang, T.; Luan, C.; Zhi, C.; Wang, P.; Huang, B.; Hong, G.; Zhang, W. Multifunctional nanodiamond interfacial layer for ultra-stable zinc-metal anodes. *Adv. Energy Mater.* **2024**, *14*, 2401479.
(21) Kang, L.; Cui, M.; Jiang, F.; Gao, Y.; Luo, H.; Liu, J.; Liang, W.; Zhi, C. Nanoporous $CaCO_3$ coatings enabled uniform Zn stripping/plating for long-life Zn rechargeable aqueous batteries. *Adv. Energy Mater.* **2018**, *8*, 1801090.
(22) Xie, X.; Liang, S.; Gao, J.; Guo, S.; Guo, J.; Wang, C.; Xu, G.; Wu, X.; Chen, G.; Zhou, J. Manipulating the ion-transfer kinetics and interface stability for high-performance Zn metal anodes. *Energy Environ. Sci.* **2020**, *13*, 503−510.
(23) Hao, J.; Li, B.; Li, X.; Zeng, X.; Zhang, S.; Yang, F.; Liu, S.; Li, D.; Wu, C.; Guo, Z. An in-depth study of Zn metal surface chemistry for advanced aqueous Zn-ion batteries. *Adv. Mater.* **2020**, *32*, 2003021.
(24) Yang, Y.; Liu, C.; Lv, Z.; Yang, H.; Zhang, Y.; Ye, M.; Chen, L.; Zhao, J.; Li, C. Synergistic manipulation of Zn^{2+} ion flux and desolvation effect enabled by anodic growth of a 3D ZnF_2 matrix for long-lifespan and dendrite-free Zn metal anodes. *Adv. Mater.* **2021**, *33*, 2007388.
(25) Zhang, L.; Zhang, B.; Zhang, T.; Li, T.; Shi, T.; Li, W.; Shen, T.; Huang, X.; Xu, J.; Zhang, X.; Wang, Z.; Hou, Y. Eliminating dendrites and side reactions via a multifunctional ZnSe protective layer toward advanced aqueous Zn metal batteries. *Adv. Funct. Mater.* **2021**, *31*, 2100186.
(26) Zhao, Z.; Zhao, J.; Hu, Z.; Li, J.; Li, j.; Zhang, Y.; Wang, C.; Cui, G. Long-life and deeply rechargeable aqueous Zn anodes enabled by a multifunctional brightener-inspired interphase. *Energy Environ. Sci.* **2019**, *12*, 1938−1949.
(27) Chen, P.; Yuan, X.; Xia, Y.; Zhang, Y.; Fu, L.; Liu, L.; Yu, N.; Huang, Q.; Wang, B.; Hu, X.; Wu, Y.; Ree, T. An artificial polyacrylonitrile coating layer confining Zn dendrite growth for highly reversible aqueous Zn-based batteries. *Adv. Sci.* **2021**, *8*, 2100309.
(28) Hao, J.; Li, X.; Zhang, S.; Yang, F.; Zeng, X.; Zhang, S.; Bo, G.; Wang, C.; Guo, Z. Designing Dendrite-Free Zn Anodes for Advanced Aqueous Zn Batteries. *Adv. Funct. Mater.* **2020**, *30*, 2001263.
(29) Li, Z.; Deng, W.; Li, C.; Wang, W.; Zhou, Z.; Li, Y.; Yuan, X.; Hu, J.; Zhang, M.; Zhu, J.; Tang, W.; Wang, X.; Li, R. Uniformizing the electric field distribution and ion migration during Zn plating/stripping via a binary polymer blend artificial interphase. *J. Mater. Chem. A* **2020**, *8*, 17725−17731.
(30) Feng, Y.; Wang, Y.; Sun, L.; Zhang, K.; Liang, J.; Zhu, M.; Tie, Z.; Jin, Z. Fluorinated interface engineering toward controllable zinc deposition and rapid cation migration of aqueous Zn-ion batteries. *Small* **2023**, *19*, 2302650.
(31) Yang, Z.; Lv, C.; Li, W.; Wu, T.; Zhang, Q.; Tang, Y.; Shao, M.; Wang, H. Revealing the two-dimensional surface diffusion mechanism for Zn dendrite formation on Zn anode. *Small* **2022**, *18*, 2104148.
(32) Zhang, W. D.; Zhang, S. Q.; Fan, L.; Gao, L. N.; Kong, X. Q.; Li, S. Y.; Li, J.; Hong, X.; Lu, Y. Y. Tuning the LUMO energy of an organic interphase to stabilize lithium metal batteries. *ACS Energy Lett.* **2019**, *4*, 644−650.
(33) Goodenough, J. B.; Kim, Y. Challenges for rechargeable Li batteries. *Chem. Mater.* **2010**, *22*, 587−603.
(34) He, H.; Qin, H.; Wu, J.; Chen, X.; Huang, R.; Shen, F.; Wu, Z.; Chen, G.; Yin, S.; Liu, J. Engineering interfacial layers to enable Zn metal anodes for aqueous zinc-ion batteries. *Energy Storage Mater.* **2021**, *43*, 317−336.
(35) Zhao, F.; Feng, J.; Dong, H.; Chen, R.; Munshi, T.; Scowen, I.; Guan, S.; Miao, Y.-E.; Liu, T.; Parkin, I. P.; He, G. Ultrathin protection layer via rapid sputtering strategy for stable aqueous zinc ion batteries. *Adv. Funct. Mater.* **2024**, *34*, 2409400.
(36) Chen, Z.-J.; Shen, T.-Y.; Zhang, M.-H.; Xiao, X.; Wang, H.-Q.; Lu, Q.-R.; Luo, Y.-L.; Jin, Z.; Li, C.-H. Tough, anti-fatigue, self-adhesive, and anti-freezing hydrogel electrolytes for dendrite-free flexible zinc ion batteries and strain sensors. *Adv. Funct. Mater.* **2024**, *34*, 2314864.
(37) Yu, J.; Lin, H.; Peng, J.; Wang, T.; Zhang, H.; Li, M.; Chu, D.; Xie, K. In situ construction of ultra-stable zincophilic sodium alginate artificial interface layer for dendrite-free anode in aqueous zinc-ion batteries. *Electrochim. Acta* **2024**, *488*, 144191.
(38) Wang, T.; Wang, P.; Pan, L.; He, Z.; Dai, L.; Wang, L.; Liu, S.; Jun, S. C.; Lu, B.; Liang, S.; Zhou, J. Stabling zinc metal anode with polydopamine regulation through dual effects of fast desolvation and ion confinement. *Adv. Energy Mater.* **2023**, *13*, 2203523.
(39) Guo, N.; Peng, Z.; Huo, W.; Li, Y.; Liu, S.; Kang, L.; Wu, X.; Dai, L.; Wang, L.; Jun, S. C.; He, Z. Stabilizing Zn metal anode through regulation of Zn ion transfer and interfacial behavior with a fast ion conductor protective layer. *Small* **2023**, *19*, 2303963.
(40) Liu, M.; Cai, J.; Ao, H.; Hou, Z.; Zhu, Y.; Qian, Y. $NaTi_2(PO_4)_3$ solid-state electrolyte protection layer on Zn metal anode for superior long-life aqueous zinc-ion batteries. *Adv. Funct. Mater.* **2020**, *30*, 2004885.
(41) Xiao, P.; Xue, L.; Guo, Y.; Hu, L.; Cui, C.; Li, H.; Zhai, T. On-site building of a Zn^{2+}-conductive interfacial layer via short-circuit energization for stable Zn anode. *Sci. Bull.* **2021**, *66*, 545−552.
(42) Zhang, B.; Huang, Y.; Gao, S.; Zhang, N.; Mei, Y.; Huang, Y.; Ding, T.; Hu, X.; Li, L.; Wu, F.; Chen, R. Uncovering diverse roles of zincophilic and hydrophobic interactions at composite interfaces to enhance the longevity of zinc-ion batteries. *J. Energy Chem.* **2025**, *107*, 908−918.
(43) Liu, P.; Zhang, Z.; Hao, R.; Huang, Y.; Liu, W.; Tan, Y.; Li, P.; Yan, J.; Liu, K. Ultra-highly stable zinc metal anode via 3D-printed g-C_3N_4 modulating interface for long life energy storage systems. *Chem. Eng. J.* **2021**, *403*, 126425.
(44) He, H.; Tong, H.; Song, X.; Song, X.; Liu, J. Highly stable Zn metal anodes enabled by atomic layer deposited Al_2O_3 coating for aqueous zinc-ion batteries. *J. Mater. Chem. A* **2020**, *8*, 7836.
(45) Gou, Q.; Chen, Z.; Luo, H.; Deng, J.; Zhang, B.; Xu, N.; Cui, J.; Zheng, Y.; Li, M.; Li, J. Synergistic modulation of mass transfer and parasitic reactions of Zn metal anode via bioinspired artificial protection layer. *Small* **2024**, *20*, 2305902.
(46) Xin, W.; Miao, L.; Zhang, L.; Peng, H.; Yan, Z.; Zhu, Z. Turning the byproduct $Zn_4(OH)_6SO_4{\cdot}xH_2O$ into a uniform solid electrolyte interphase to stabilize aqueous Zn anode. *ACS Materials Lett.* **2021**, *3*, 1819−1825.
(47) Wang, Y.; Liao, X.; Wang, W.; Chen, S.; Chen, J.; Wang, H. Direct growth of a polymer film to induce horizontal orientation of $Zn_4(OH)_6SO_4{\cdot}xH_2O$ for stable Zn metal batteries. *ACS Appl. Mater. Interfaces* **2024**, *16*, 14912−14921.

https://doi.org/10.1021/acsenergylett.5c02939
ACS Energy Lett. 2025, 10, 6489−6499

(48) Tian, H.; Feng, G.; Wang, Q.; Li, Z.; Zhang, W.; Lucero, M.; Feng, Z.; Wang, Z.-L.; Zhang, Y.; Zhen, C.; Gu, M.; Shan, X.; Yang, Y. Three-dimensional Zn-based alloys for dendrite-free aqueous Zn battery in dual-cation electrolytes. *Nature Commun.* **2022**, *13*, 7922.
(49) Zhang, N.; Dong, Y.; Jia, M.; Bian, X.; Wang, Y.; Qiu, M.; Xu, J.; Liu, Y.; Jiao, L.; Cheng, F. Rechargeable aqueous Zn−V_2O_5 battery with high energy density and long cycle life. *ACS Energy Lett.* **2018**, *3*, 1366−1372.
(50) Senguttuvan, P.; Han, S.-D.; Kim, S.; Lipson, A. L.; Tepavcevic, S.; Fister, T. T.; Bloom, I. D.; Burrell, A. K.; Johnson, C. S. A high power rechargeable nonaqueous multivalent Zn/V_2O_5 battery. *Adv. Energy Mater.* **2016**, *6*, 1600826.
(51) Yan, C.; Zhu, L.; Li, P.; Tang, J.; He, H.; Zhu, Y.; Li, D. Multi-level Zn^{2+}-buffering interphase enabled by hierarchical nanostructure engineering of gel polymers for highly reversible zinc metal anode. *Adv. Mater.* **2025**, No. e15316.
(52) Hieu, L. T.; So, S.; Kim, I. T.; Hur, J. Zn anode with flexible β-PVDF coating for aqueous Zn-ion batteries with long cycle life. *Chem. Eng. J.* **2021**, *411*, 128584.
(53) Liang, P.; Yi, J.; Liu, X.; Wu, K.; Wang, Z.; Cui, J.; Liu, Y.; Wang, Y.; Xia, Y.; Zhang, J. Highly reversible Zn anode enabled by controllable formation of nucleation sites for Zn-based batteries. *Adv. Funct. Mater.* **2020**, *30*, 1908528.
(54) Chen, W.; Tang, J.; Ji, F.; Sun, J.; Zhu, Q.; Liu, B.-T. A multifunctional gradient coating enables dendrite-free and side reaction-free zinc anodes for stable zinc-ion batteries. *Cell Rep. Phys. Sci.* **2023**, *4*, 101344.
(55) Lu, J.; Yang, J.; Zhang, Z.; Wang, C.; Xu, J.; Wang, T. Silk fibroin coating enables dendrite-free zinc anode for long-life aqueous zinc-ion batteries. *ChemSusChem* **2022**, *15*, No. e202200656.
(56) Dong, X.; Peng, Y.; Wang, Y.; Wang, H.; Jiang, C.; Huang, C.; Meng, C.; Zhang, Y. Hemimorphite/C interface layer with dual-effect methodically redistricted Zn^{2+} deposition behavior for dendrite-free Zinc metal anodes. *Energy Storage Mater.* **2023**, *62*, 102937.
(57) Zhang, M.; Li, J.-H.; Tang, Y.; Wang, D.-W.; Hu, H.; Liu, M.; Xiao, B.; Wang, P.-F. Selective Zn-ion channels enabled by a double-network protective layer for stable zinc anode. *Energy Storage Mater.* **2024**, *65*, 103113.
(58) Kang, L.; Zheng, J.; Yue, K.; Yuan, H.; Luo, J.; Wang, Y.; Liu, Y.; Nai, J.; Tao, X. Amino-functionalized interfacial layer enables an ultra-uniform amorphous solid electrolyte interphase for high-performance aqueous zinc-based batteries. *Small* **2023**, *19*, 2304094.

https://doi.org/10.1021/acsenergylett.5c02939
ACS Energy Lett. 2025, 10, 6489−6499